



## Ti<sub>3</sub>C<sub>2</sub>T<sub>x</sub> MXene as a Janus cocatalyst for concurrent promoted photoactivity and inhibited photocorrosion

Xiuqiang Xie<sup>a,b</sup>, Nan Zhang<sup>a,b</sup>, Zi-Rong Tang<sup>b</sup>, Masakazu Anpo<sup>a,c</sup>, Yi-Jun Xu<sup>a,b,\*</sup>

<sup>a</sup> State Key Laboratory of Photocatalysis on Energy and Environment, College of Chemistry, Fuzhou University, Fuzhou 350116, PR China

<sup>b</sup> College of Chemistry, New Campus, Fuzhou University, Fuzhou 350116, PR China

<sup>c</sup> Department of Applied Chemistry, Graduate School of Engineering, Osaka Prefecture University, Osaka 599-8531, Japan



### ARTICLE INFO

#### Keywords:

Ti<sub>3</sub>C<sub>2</sub>T<sub>x</sub> MXene  
Janus cocatalyst  
Photocorrosion  
2D heterostructures

### ABSTRACT

Employing a single cocatalyst to concurrently mediate reactions with electrons and those with holes toward efficient and stable photocatalysts is highly desirable yet challenging. Herein, two-dimensional (2D) in-plane CdS/Ti<sub>3</sub>C<sub>2</sub>T<sub>x</sub> sheet-onto-sheet heterostructures have been deliberately constructed, in which Ti<sub>3</sub>C<sub>2</sub>T<sub>x</sub>, a prototype MXene, is demonstrated to act as a Janus cocatalyst for simultaneously promoting electron-driven photoreduction reaction and inhibiting hole-induced photocorrosion of semiconductor CdS. Ti<sub>3</sub>C<sub>2</sub>T<sub>x</sub> serves as an electron mediator to boost the electron extraction from CdS for photoreduction reactions. The interlayer assembly maintains the accessible surface reaction sites of CdS, while concomitantly the Cd<sup>2+</sup> confinement effect of Ti<sub>3</sub>C<sub>2</sub>T<sub>x</sub> retards the oxidative holes induced photocorrosion of CdS through preventing Cd<sup>2+</sup> leaching. As a result, the photoactivity and stability of CdS are concurrently enhanced through coupling with Ti<sub>3</sub>C<sub>2</sub>T<sub>x</sub> as a Janus cocatalyst. This facile and double-gain strategy is expected to present a conceptual approach to the rational design of efficient and stable photocatalysts toward solar energy conversion.

### 1. Introduction

Photocatalysis based on semiconductors has been continuously pursued to relieve the looming environmental and energy crisis, which in principle utilizes photogenerated charge carriers to realize solar-to-chemical energy conversion [1–6]. However, side reactions of charge carriers, such as the electron-hole recombination and the undesired photocorrosion induced by holes, compete with photocatalytic processes, which significantly challenge efficient and durable photocatalysis [7,8]. Consequently, it is essential to concurrently mediate reaction pathways of photogenerated electrons and holes to (i) maximize their overall efficiency of participation in the target redox reactions while suppressing their recombination, and (ii) minimize the engagement of holes in photocorrosion reactions to improve the stability of photocatalysts. In this regard, the introduction of appropriate dual cocatalysts with accumulative catalytic effects as spatially separated trapping sites for electrons and holes has proven to be efficient [9–11]. Noteworthily, it often involves stepwise procedures and requires spatially separated deposition of two distinct cocatalysts. It is highly desirable to employ a single cocatalyst with integrated functionalities to simultaneously mediate the photoredox reactions with electrons and those with holes for efficient and stable photocatalysts.

CdS represents a model semiconductor photocatalyst, which exhibits excellent solar spectral response and thermodynamically favorable energy levels to drive a broad spectrum of photocatalytic reactions [12–20]. However, besides the general issue of electron-hole recombination limiting the photoactivity that occurs in most photocatalysts, the photogenerated holes induced photocorrosion causes the deactivation of CdS and secondary pollution of Cd<sup>2+</sup> leaching, which has been the Achilles' heel of CdS-based photocatalysis [21,22]. In this realm, conspicuous efforts have been made, which can be classified into two aspects. One is to focus on the spatial transfer/depletion of the holes to slow down the photocorrosion of CdS, such as elaborating CdS-based heterojunctions [12,15,17,22], introducing hole-conducting cocatalysts [21,23,24], and hole scavengers [25–28]. The other is to artificially control the conditions that can retard the photocorrosion reaction of CdS, such as coating poly(diallyl dimethylammonium) chloride over CdS to prevent the leakage of Cd<sup>2+</sup> to the reaction medium [29], and draping graphene layers over a CdS electrode to isolate CdS from the destructive O<sub>2</sub>/H<sub>2</sub>O [30]. Although significant progress has been achieved through these approaches, some critical issues remain to be addressed. For example, the photogenerated holes transfer from the bulk of CdS to the surface is generally rate-limiting [31–33], which could eventually lead to the intrinsic photocorrosion of

\* Corresponding author at: State Key Laboratory of Photocatalysis on Energy and Environment, College of Chemistry, Fuzhou University, Fuzhou 350116, PR China.  
E-mail address: [yjxu@fzu.edu.cn](mailto:yjxu@fzu.edu.cn) (Y.-J. Xu).

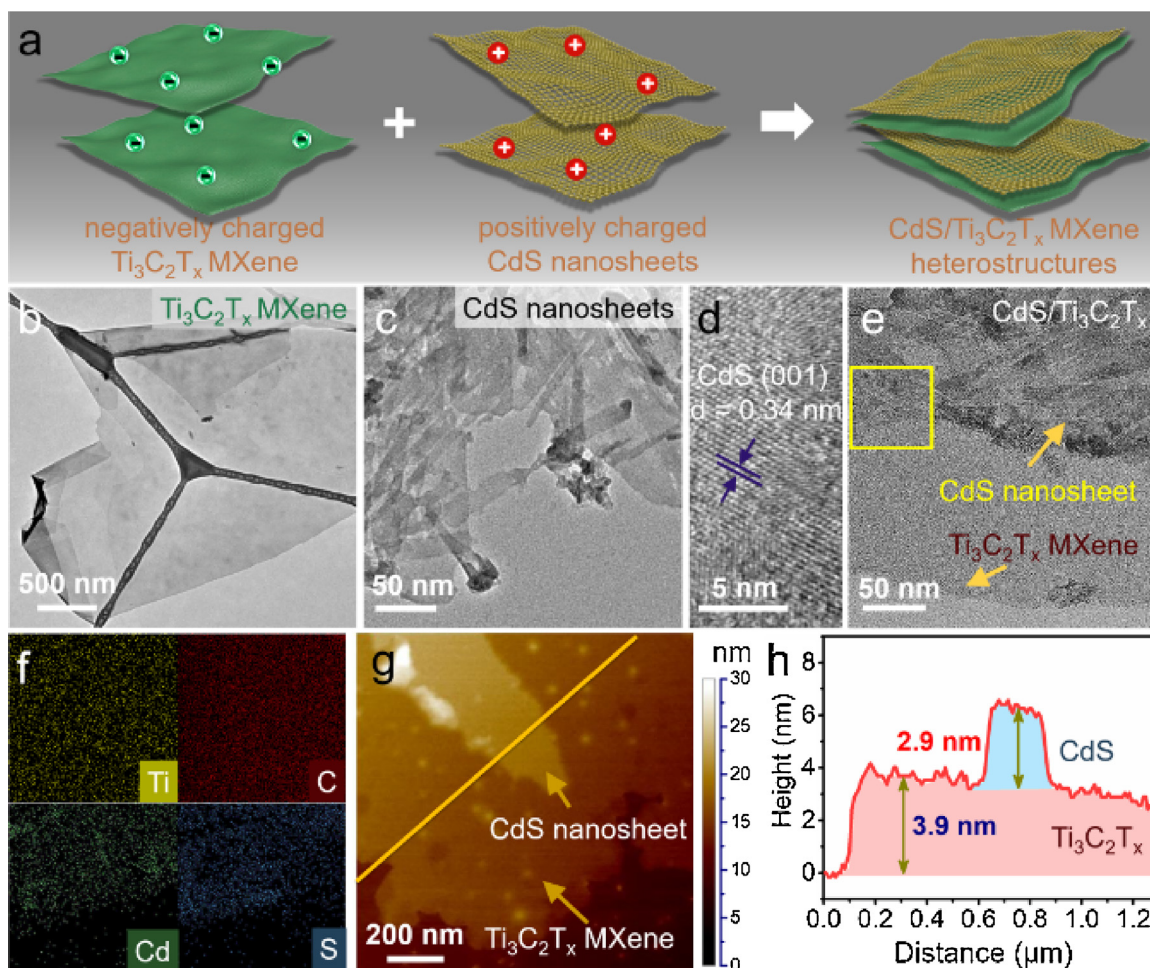


**Fig. 1.** (a) Schematic preparation of  $\text{CdS}/\text{Ti}_3\text{C}_2\text{T}_x$  heterostructures. (b) TEM image of  $\text{Ti}_3\text{C}_2\text{T}_x$  nanosheet. (c) TEM and (d) HRTEM images of the pure CdS nanosheets. (e) TEM image of the as-prepared 2D  $\text{CdS}/\text{Ti}_3\text{C}_2\text{T}_x$  sheet-onto-sheet heterostructures. (f) The corresponding elemental mapping images for the selected area (yellow rectangle in (e)). (g) AFM image and (h) the corresponding height profile of  $\text{CdS}/\text{Ti}_3\text{C}_2\text{T}_x$  heterostructures. (For interpretation of the references to colour in this figure legend, the reader is referred to the web version of this article.)

CdS and restrict the anti-photocorrosion capability of the former strategies [34,35]. As for the later ones, the introduced physical barriers inevitably block surface active sites of CdS, which could compromise the photoactivity. Therefore, enhancing the photocorrosion resistance of CdS but without shielding the active sites is a key issue to be solved. In this sense, using a single cocatalyst to concurrently mediate reaction pathways of electrons and retard the hole-induced photocorrosion without sacrificing surface active sites represents an attractive goal toward efficient and stable CdS-based photocatalysts.

Two-dimensional (2D) metal carbides, carbonitrides and nitrides, denoted as MXenes with a general formula of  $\text{M}_{n+1}\text{X}_n\text{T}_x$  (M, X, and T stand for transition metal, carbon/nitrogen, and surface terminations such as OH, O, and F, respectively), have been attracting enormous attention, among which  $\text{Ti}_3\text{C}_2\text{T}_x$  is a prototype one with high metallic conductivity and rich surface properties [36,37]. It has been reported that  $\text{Ti}_3\text{C}_2\text{T}_x$  MXene possesses favourable Fermi level position and high electrical conductivity, which enables it as an efficient cocatalyst to facilitate the separation and transfer of photogenerated charge carriers, thereby promoting the photocatalytic performance of metal sulfides [38]. In this work, we have adopted  $\text{Ti}_3\text{C}_2\text{T}_x$  as a 2D platform to construct in-plane  $\text{CdS}/\text{Ti}_3\text{C}_2\text{T}_x$  sheet-onto-sheet heterostructures. The 2D-2D coupling has been proven to be efficient as compared to other composites with different dimensionality (e.g., 0D-2D and 1D-2D) [2,39,40], which not only maximizes the  $\text{CdS}-\text{Ti}_3\text{C}_2\text{T}_x$  interlayer interaction, but also ensures open surface reaction sites for photocatalysis. With the contribution of  $\text{Ti}_3\text{C}_2\text{T}_x$  as an electron mediator, the improved

extraction of photogenerated electrons to participate in photoreduction reactions has been achieved. Simultaneously, by virtue of the strong interaction between  $\text{Cd}^{2+}$  and  $\text{Ti}_3\text{C}_2\text{T}_x$ ,  $\text{Cd}^{2+}$  ions released from CdS photocorrosion are *in situ* confined on the interlayer interacted  $\text{Ti}_3\text{C}_2\text{T}_x$ , preventing  $\text{Cd}^{2+}$  leaching without compromising surface reaction sites and thus leading to the photocorrosion resistance of CdS. These merits endow  $\text{Ti}_3\text{C}_2\text{T}_x$  as a Janus cocatalyst to concurrently regulate the reduction reactions with electrons and the photocorrosion induced by the holes, synergistically leading to CdS-based photocatalysts with enhanced performance and stability.

## 2. Experimental section

### 2.1. Preparation of the pristine CdS nanosheets

0.32 mmol  $\text{CdCl}_2 \cdot 2.5\text{H}_2\text{O}$ , 2.0 mmol S powder and 12 mL of diethylenetriamine (DETA) were mixed and vigorously stirred to form a homogeneous suspension [41]. The mixture was then hydrothermally treated at 80 °C for 48 h. After being cooled down to room temperature naturally, the precipitate was collected by centrifugation and washed with ethanol and DI water. The as-obtained CdS were dried in an oven at 60 °C for 24 h and the pristine CdS nanosheets were obtained.

### 2.2. Preparation of APTES-treated CdS nanosheets

The pristine CdS nanosheets were dispersed in 30 mL of ethanol,

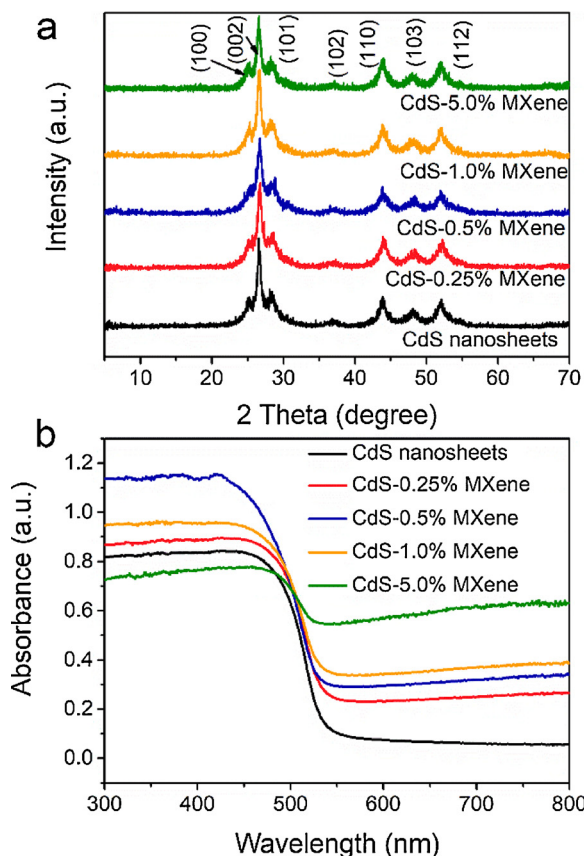


**Fig. 2.** (a) XRD patterns and (b) DRS spectra of the pure CdS nanosheets and CdS/Ti<sub>3</sub>C<sub>2</sub>T<sub>x</sub> heterostructures.

into which 0.15 mL of (3-aminopropyl) triethoxysilane (APTES) was added. After that, the mixture was heated at 60 °C for 4 h. The APTES-treated CdS were sufficiently rinsed with ethanol and APTES-treated CdS nanosheets were obtained after drying at 60 °C for 24 h.

### 2.3. Synthesis of Ti<sub>3</sub>C<sub>2</sub>T<sub>x</sub> MXene nanosheets

Ti<sub>3</sub>C<sub>2</sub>T<sub>x</sub> MXene nanosheets colloid was prepared as described previously [42,43]. In detail, multilayered Ti<sub>3</sub>C<sub>2</sub>T<sub>x</sub> was firstly synthesized by etching 1 g Ti<sub>3</sub>AlC<sub>2</sub> powders in a mixture of 1 g lithium fluoride and 10 mL hydrochloric acid (9 mol L<sup>-1</sup>) for 24 h at 35 °C. The product was washed with deionized water until the pH of the supernatant was above 5. The multilayered Ti<sub>3</sub>C<sub>2</sub>T<sub>x</sub> powder was then added into 200 mL deionized water and delaminated by bath sonication for 1 h under Ar flow. After centrifugation for 1 h at 3500 rpm, the dark green supernatant was collected. The concentration of the delaminated Ti<sub>3</sub>C<sub>2</sub>T<sub>x</sub> was determined by filtering a known volume of the supernatant through a Celgard membrane and measuring the weight of the film after drying. The delaminated Ti<sub>3</sub>C<sub>2</sub>T<sub>x</sub> colloid was then diluted to obtain a concentration of 0.5 mg mL<sup>-1</sup>.

### 2.4. Synthesis of CdS/Ti<sub>3</sub>C<sub>2</sub>T<sub>x</sub> heterostructures by electrostatic assembly

CdS/Ti<sub>3</sub>C<sub>2</sub>T<sub>x</sub> heterostructures were prepared through an electrostatic self-assembly process. Typically, the APTES-treated CdS nanosheets were dispersed in water with a concentration of 0.5 mg mL<sup>-1</sup> by ultrasonication. Ti<sub>3</sub>C<sub>2</sub>T<sub>x</sub> colloid (0.5 mg mL<sup>-1</sup>) was then added into the as-prepared APTES-treated CdS nanosheets solution and stirred at room temperature for 1 h. Subsequently, the mixture was centrifuged and washed with DI water. The precipitate obtained was dried in an oven at 60 °C to get CdS/Ti<sub>3</sub>C<sub>2</sub>T<sub>x</sub> heterostructures.

### 2.5. Materials characterizations

Zeta potentials ( $\xi$ ) of the samples were determined by dynamic light scattering analysis (Zeta sizer 3000HSA) at room temperature. X-ray diffraction (XRD) measurements were conducted on a MiniFlex 600 X-ray diffractometer (40 kV, 20 mA) using Ni-filtered Cu K $\alpha$  radiation at a scan rate of 0.1° s<sup>-1</sup>. Transmission electron microscopy (TEM) images and elemental mapping results were obtained using a JEOL model JEM 2010 EX instrument at an acceleration voltage of 200 kV. Ultraviolet-visible (UV-vis) diffuse reflectance spectra (DRS) were recorded on a Cary-500 UV-vis-NIR spectrometer and BaSO<sub>4</sub> powder was used as the internal standard to obtain the optical properties of the samples. X-ray photoelectron spectroscopy (XPS) measurements were carried out on a Thermo Scientific ESCA Lab 250 spectrometer, which consists of monochromatic Al K $\alpha$  as the X-ray source, a hemispherical analyzer, and a sample stage with multiaxial adjustability. Micromeritics ASAP 3020 equipment was used to determine the nitrogen adsorption-desorption isotherms and the Brunauer–Emmett–Teller (BET) surface areas at 77 K. The samples were degassed at 180 °C for 3 h and then analyzed at 77 K. The relative pressure (P/P<sub>0</sub>) range used for the calculation of BET surface area was from 0.05 to 0.35. The photoluminescence spectra (PL) for powder samples were analyzed on an Edinburgh Analytical Instrument F900 spectrophotometer with an excitation wavelength of 400 nm. To ensure the comparability of the PL spectra, the experimental parameters, including the excitation wavelength, slit width, and the amount of the samples, were identical. The concentration of Cd<sup>2+</sup> was quantified by an inductively coupled plasma emission spectroscopy instrument (ICP, PerkinElmer Optima 2000DV). Atomic force microscopy (AFM) measurements were performed on a Dimension Icon (Bruker) using a tapping mode. The sample was deposited on a mica piece for AFM measurements. The electrical conductivity measurement of Ti<sub>3</sub>C<sub>2</sub>T<sub>x</sub> MXene nanosheets was performed by measuring the resistivity–pressure curve (R–P curve) using a four-point probe technique on a ST2722 (Suzhou Jingge Electronic Co., People's Republic of China) power resistivity tester.

Photoelectrochemical measurements were performed in a homemade three electrode quartz cell using an Autolab electrochemical workstation. A Pt plate was used as the counter electrode, and Ag/AgCl electrode was used as the reference electrode. The working electrode was prepared on fluorine-doped tin oxide (FTO) glasses cleaned by ultrasonication in ethanol for 30 min and dried at 80 °C. Typically, 5 mg of the sample was dispersed in 0.5 mL of ethanol to get a slurry by ultrasonication. The slurry was spread onto FTO glass, whose side part was previously protected by Scotch tape. The Scotch tape was then unstuck, and the uncoated part of the electrode was isolated with epoxy resin. The exposed area of the working electrode was 0.25 cm<sup>2</sup>. The electrochemical impedance spectroscopy (EIS) measurement was carried out in the three electrode cell in a KCl solution (0.5 M) containing 0.01 mM K<sub>3</sub>[Fe(CN)<sub>6</sub>]/K<sub>4</sub>[Fe(CN)<sub>6</sub>] (1:1) under open circuit potential conditions. The photocurrent measurement was conducted without voltage bias and the electrolyte was 0.2 M aqueous Na<sub>2</sub>SO<sub>4</sub> solution (pH = 6.8). The visible light irradiation source was a 300 W Xe arc lamp system equipped with a UV-CUT filter ( $\lambda \geq 420$  nm). The cathodic polarization curves were obtained using the linear sweep voltammetry (LSV) technique with a scan rate of 0.2 mV s<sup>-1</sup> in 0.1 M Na<sub>2</sub>SO<sub>4</sub> aqueous solution. The CV analysis was performed in 0.5 M KCl solution containing 5.0 mM K<sub>3</sub>[Fe(CN)<sub>6</sub>]/K<sub>4</sub>[Fe(CN)<sub>6</sub>] with a scan rate of 0.1 V s<sup>-1</sup>. The OCPD measurements were conducted in 0.1 M Na<sub>2</sub>SO<sub>4</sub> aqueous solution by visible light irradiation for 120 s and then monitored the subsequent decay of photovoltage for 130 s with light turned off.

### 2.6. Photocatalytic activity tests

In a typical photocatalytic reaction, a 300 W Xe arc lamp (PLS-SXE

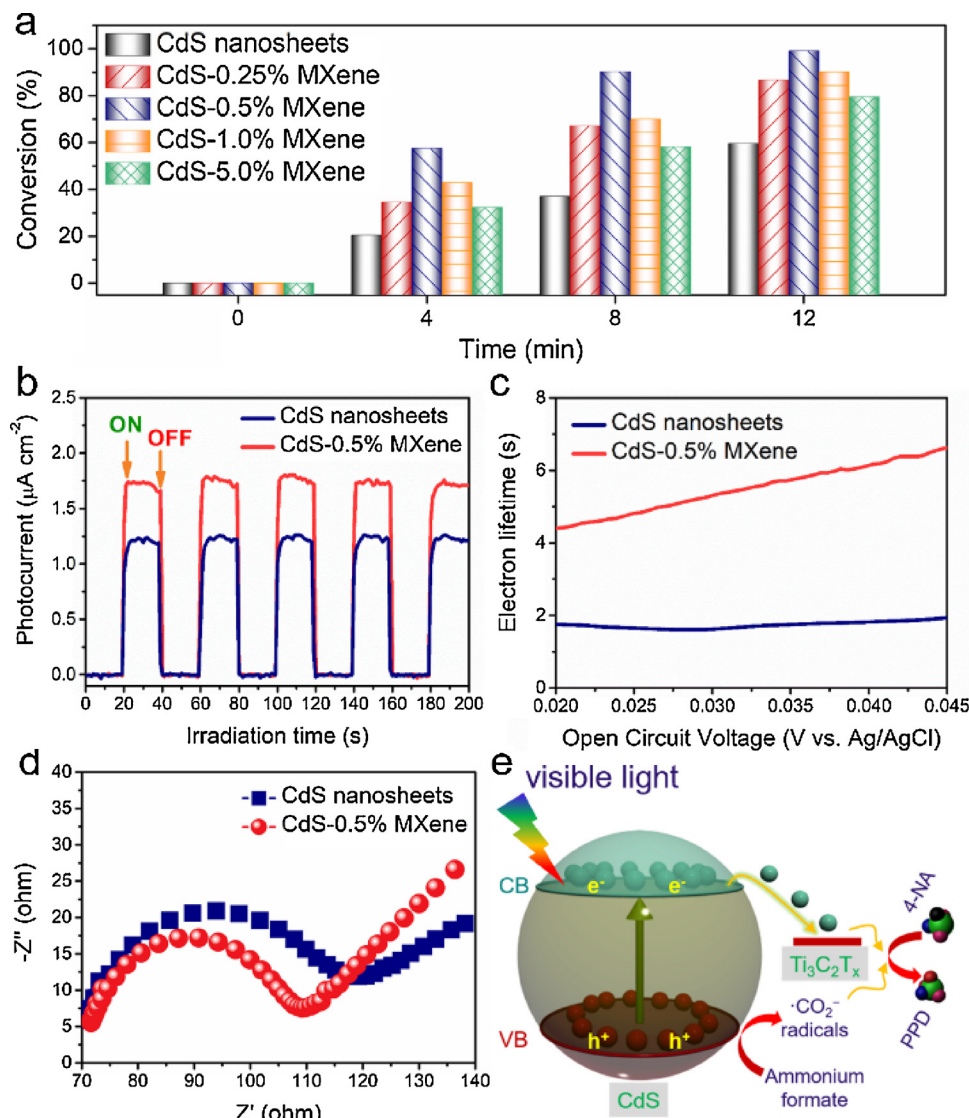


**Fig. 3.** (a) Photocatalytic selective reduction of 4-NA over the pure CdS nanosheets, and CdS/Ti<sub>3</sub>C<sub>2</sub>T<sub>x</sub> heterostructures under visible light irradiation ( $\lambda \geq 420$  nm). (b) Photocurrent densities, (c) electron lifetimes, and (d) Nyquist plots of the pure CdS nanosheets and CdS-0.5% MXene electrodes. (e) Mechanism of photoreduction of 4-NA over CdS/Ti<sub>3</sub>C<sub>2</sub>T<sub>x</sub>.

300, Beijing Perfect light Co., Ltd.) with a UV-CUT filter ( $\lambda \geq 420$  nm) was used as the irradiation source. The incident light power density is 383 mW cm<sup>-2</sup>. 15 mg of the samples and 40 mg of ammonium formate were added into 30 mL of the aromatic nitro compounds solution (20 mg L<sup>-1</sup>) in a quartz vial. Before visible light illumination, the above suspension was stirred in the dark for 1 h to ensure the establishment of adsorption–desorption equilibrium between the sample and reactants. During the process of the reaction, 3 mL of sample solution was collected at a certain time interval and centrifuged to remove the catalyst completely at 10,000 rpm. Afterward, the solution was analyzed on a Varian ultraviolet–visible light (UV–vis) spectrophotometer (Cary-50, Varian Co.). The whole experimental process was conducted under N<sub>2</sub> purging at a flow rate of 80 mL min<sup>-1</sup>. Control experiments were carried out similar to the above photocatalytic selective reduction of nitro organics except the controlled reaction conditions.

#### 2.7. Evaluation of adsorption properties

The adsorption of 4-NA over CdS-0.5% MXene and the pure CdS nanosheets were performed similar to the photocatalytic activity tests except the visible light irradiation process and the concentrations of 4-

NA were analyzed by a Varian ultraviolet–visible light (UV–vis) spectrophotometer (Cary-50, Varian Co.). The adsorption of Cd<sup>2+</sup> over CdS nanosheets and Ti<sub>3</sub>C<sub>2</sub>T<sub>x</sub> MXene was performed by adding 10 mg of CdS nanosheets or Ti<sub>3</sub>C<sub>2</sub>T<sub>x</sub> in 50 mL of Cd<sup>2+</sup> solution (10 ppm). During the process of the adsorption, 4 mL of solution was collected at a certain time interval. To remove the sample completely, the solution was filtered through a syringe filter (0.22 μm pore size, Tianjin Jinteng) and then centrifuged at 10,000 rpm. Afterward, the concentration of Cd<sup>2+</sup> was measured by ICP.

#### 3. Results and discussion

2D CdS/Ti<sub>3</sub>C<sub>2</sub>T<sub>x</sub> heterostructures have been constructed by an electrostatic assembly strategy (Fig. 1a), which circumvents the requirement of lattice matching of CdS and Ti<sub>3</sub>C<sub>2</sub>T<sub>x</sub> for assembling in-plane heterostructures. Ti<sub>3</sub>C<sub>2</sub>T<sub>x</sub> nanosheets have been successfully prepared according to the previous literature [43], as evidenced by the X-ray diffraction (XRD) pattern (Fig. S1) and the transmission electron microscopy (TEM) image (Fig. 1b). The typical 2D morphology of the CdS nanosheets has been revealed by the TEM image (Fig. 1c). The high-resolution TEM (HRTEM) image in Fig. 1d clearly shows the lattice

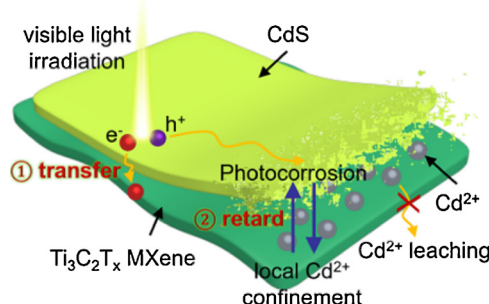
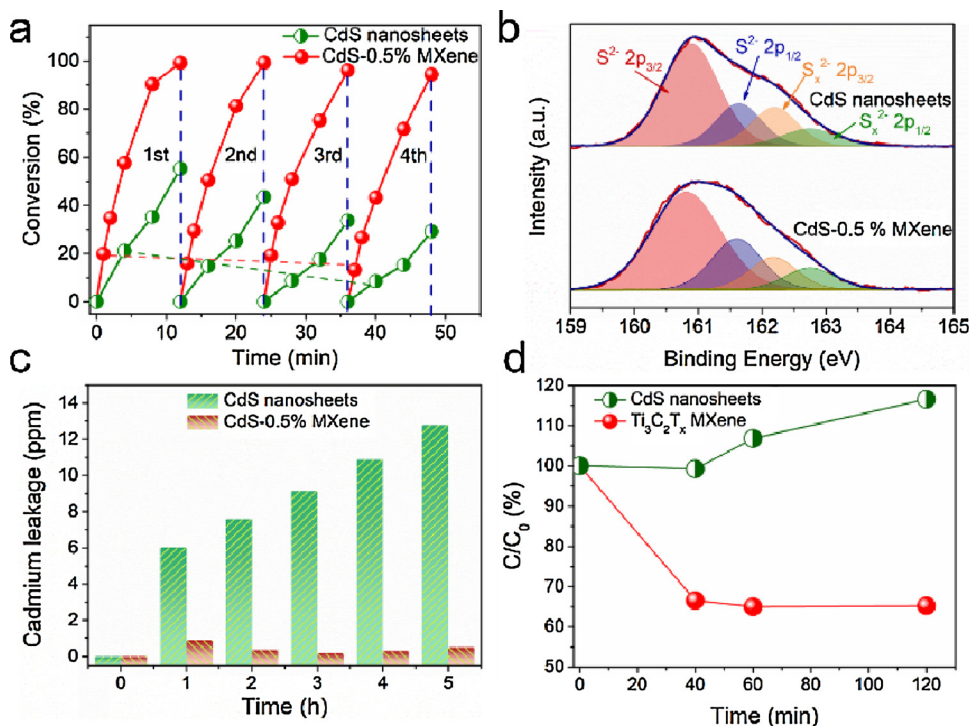


Fig. 5. Schematic illustration of Ti<sub>3</sub>C<sub>2</sub>T<sub>x</sub> enhanced photostability of CdS.

spacing of 0.34 nm, which is attributed to the (001) crystal plane of the hexagonal CdS. Both the Ti<sub>3</sub>C<sub>2</sub>T<sub>x</sub> and the pristine CdS nanosheets are negatively charged with zeta potentials of  $-31.8\text{ mV}$  (Fig. S2) and  $-14\text{ mV}$  (Fig. S3), respectively. To realize the electrostatic assembly, the CdS nanosheets have been modified by 3-aminopropyl-triethoxysilane (APTES), producing positively charged CdS nanosheets with a zeta potential of  $+5.8\text{ mV}$  (Fig. S4). After a simple liquid-phase mixing, interlayer assembly between the positively charged CdS nanosheets and the negatively charged Ti<sub>3</sub>C<sub>2</sub>T<sub>x</sub> nanosheets occurs readily due to the electrostatic attractions, which is accompanied by the appearance of ensembles quickly (Fig. S5). As such, 2D in-plane CdS/Ti<sub>3</sub>C<sub>2</sub>T<sub>x</sub> heterostructures are produced, as indicated by the TEM image shown in Fig. 1e. The elemental mapping results further confirm the 2D CdS-on-Ti<sub>3</sub>C<sub>2</sub>T<sub>x</sub> structure with CdS nanosheets well stacked on the 2D mat of Ti<sub>3</sub>C<sub>2</sub>T<sub>x</sub> (Fig. 1f). The in-plane CdS/Ti<sub>3</sub>C<sub>2</sub>T<sub>x</sub> heterostructures have also been investigated by atomic force microscopy (AFM) characterization shown in Fig. 1g, which reveals the same CdS-on-Ti<sub>3</sub>C<sub>2</sub>T<sub>x</sub> morphology as the TEM observation. As shown in Fig. 1h, the thicknesses of Ti<sub>3</sub>C<sub>2</sub>T<sub>x</sub> and CdS nanosheets are about 3.9 and 2.9 nm, respectively. The TEM and AFM results clearly demonstrate that the 2D in-plane CdS/Ti<sub>3</sub>C<sub>2</sub>T<sub>x</sub> sheet-onto-sheet heterostructures with intimate interfacial contact have been successfully achieved, which maximize the interactions between CdS and Ti<sub>3</sub>C<sub>2</sub>T<sub>x</sub> 2D nanosheets. In addition, such 2D in-plane heterostructures maintain exposed surface of CdS, which is desired for

Fig. 4. (a) Photostability of the pure CdS nanosheets and CdS-0.5% MXene for the photo-reduction of 4-NA. (b) High resolution XPS spectra of S 2p for the used pure CdS nanosheets and CdS-0.5% MXene after photocatalytic reduction of 4-NA. (c) Cd<sup>2+</sup> leakage profiles under visible light irradiation. (d) Adsorption of Cd<sup>2+</sup> over CdS nanosheets and Ti<sub>3</sub>C<sub>2</sub>T<sub>x</sub> MXene in the dark.

photocatalytic reactions.

CdS/Ti<sub>3</sub>C<sub>2</sub>T<sub>x</sub> heterostructures with different weight ratios of Ti<sub>3</sub>C<sub>2</sub>T<sub>x</sub> MXene (denoted as CdS-x MXene,  $x = 0.25, 0.5, 1.0$ , and  $5.0\%$ , respectively) display virtually identical XRD patterns to that of the pure CdS nanosheets, and no diffraction peak for Ti<sub>3</sub>C<sub>2</sub>T<sub>x</sub> can be observed (Fig. 2a) due to the low weight ratio and homogeneous dispersion of Ti<sub>3</sub>C<sub>2</sub>T<sub>x</sub> in the heterostructures. Specifically, the peaks located at *ca.* 24.8, 26.5, 28.2, 36.6, 43.7, 47.9, and 51.8° are distinctly indexed to the (100), (002), (101), (102), (110), (103), and (112) crystal planes of CdS (JCPDS No. 77-2306) with a hexagonal phase, respectively. N<sub>2</sub> adsorption-desorption measurements indicate that the CdS/Ti<sub>3</sub>C<sub>2</sub>T<sub>x</sub> heterostructures have the similar surface areas and pore volumes to that of the pure CdS nanosheets (Table S1). Diffused reflectance spectra (DRS) suggest that CdS/Ti<sub>3</sub>C<sub>2</sub>T<sub>x</sub> hybrids show enhanced absorption spectra in the visible light region compared to the pure CdS nanosheets because of the background light absorption of Ti<sub>3</sub>C<sub>2</sub>T<sub>x</sub> (Fig. 2b).

To verify whether the introduction of Ti<sub>3</sub>C<sub>2</sub>T<sub>x</sub> MXene with a high electrical conductivity (Fig. S6) can promote the extraction of photo-generated electrons from CdS, selective photocatalytic reduction of 4-nitroaniline (4-NA) in aqueous phase as a probe reaction has been performed under visible light irradiation ( $\lambda \geq 420\text{ nm}$ ), with N<sub>2</sub> purging and ammonium formate as scavenger of photogenerated holes. Fig. 3a demonstrates that the introduction of Ti<sub>3</sub>C<sub>2</sub>T<sub>x</sub> effectively enhances the photoactivity of CdS toward the photoreduction of 4-NA to *p*-phenylenediamine (PPD) (Fig. S7). This chemical transformation is attractive considering that PPD is an important intermediate for the synthesis of dyes, rubber antioxidants and aramid textile fiber in chemical industry [28]. It is noted that pure Ti<sub>3</sub>C<sub>2</sub>T<sub>x</sub> exhibits negligible photoactivity toward the photoreduction of 4-NA (Fig. S8), suggesting that CdS is the photoactive component in CdS/Ti<sub>3</sub>C<sub>2</sub>T<sub>x</sub> composites. The optimum Ti<sub>3</sub>C<sub>2</sub>T<sub>x</sub> weight addition ratio is 0.5% and further increasing the loading amount of Ti<sub>3</sub>C<sub>2</sub>T<sub>x</sub> results in a deterioration of activity, which might be ascribed to the “light-shielding effect” of Ti<sub>3</sub>C<sub>2</sub>T<sub>x</sub>. The optimum CdS-0.5% MXene also exhibits enhanced photoactivity compared to the pure CdS nanosheets toward the reduction of other aromatic nitro compounds with different substituent groups, such as 4-chloronitrobenzene, 4-nitrophenol, 4-nitrotoluene, 4-bromonitrobenzene, and 4-nitroanisole (Fig. S9).

Control experiments have been conducted to investigate the mechanism of the photocatalytic reduction of 4-NA. As shown in Fig. S10, no conversion of 4-NA has been observed without light irradiation or photocatalysts, verifying that the reduction of 4-NA is driven by the photocatalytic process over CdS/MXene. The conversion of 4-NA is significantly decreased without N<sub>2</sub> purging, suggesting that an anaerobic atmosphere by N<sub>2</sub> purging is crucial for the efficient photocatalytic reduction of 4-NA. It has been demonstrated that ammonium formate easily quenches photogenerated holes and generates ·CO<sub>2</sub>-radicals with strong reductive potential (·CO<sub>2</sub>/CO<sub>2</sub>, -1.8 V vs. RHE), which can reduce 4-NA to PPD (4-NA/PPD, -0.3 V vs. RHE) [44,45]. As a result, without ammonium formate, the photocatalytic conversion of 4-NA is decreased to 32.8% over the optimum CdS-0.5% MXene (Fig. S10). When adding K<sub>2</sub>S<sub>2</sub>O<sub>8</sub> as the scavenger for photogenerated electrons, the conversion of 4-NA is only 9.9%, which is much lower than that in the absence of ammonium formate. Consequently, the decisive factor for the effective photoreduction of 4-NA is photogenerated electrons. In addition, the adsorption capabilities of CdS-0.5% MXene and the pure CdS nanosheets toward 4-NA are found to be similar (Fig. S11). This result in combination with the control experiments suggests that the enhanced photocatalytic performance of CdS/Ti<sub>3</sub>C<sub>2</sub>T<sub>x</sub> heterostructures compared to the CdS nanosheets is attributed to the improved surface reactions with electrons rather than adsorptivities.

Fig. 3b shows the on-off transient photocurrent responses of the pure CdS nanosheets and the CdS-0.5% MXene under visible light irradiation ( $\lambda \geq 420$  nm) without bias. Evidently, CdS-0.5% MXene exhibits increased photocurrent compared to the pure CdS, indicating that the separation of photogenerated charge carriers over CdS-0.5% MXene is more efficient than that over the CdS nanosheets. This is further confirmed by the weaker photoluminescence (PL) intensity of CdS-0.5% MXene than the pure CdS nanosheets (Fig. S12), suggesting the efficient inhibition of electron-hole pair recombination by MXene introduction. Lifetime of photoelectrons has been measured by open circuit photovoltage ( $V_{oc}$ ) decay (OCPD) technique [46]. The calculated electron lifetime as a function of  $V_{oc}$  is shown in Fig. 3c, from which it is clearly seen that photoelectron lifetime of CdS-0.5% MXene is much longer than that of the CdS nanosheets. These results signify that Ti<sub>3</sub>C<sub>2</sub>T<sub>x</sub> significantly reduces the recombination of photogenerated electron-hole pairs and prolongs the lifetime of charge carriers, which can be ascribed to the lower Femi level of Ti<sub>3</sub>C<sub>2</sub>T<sub>x</sub> than the conduction band (CB) of CdS [38]. In addition, as evidenced by the Nyquist plots displayed in Fig. 3d, the CdS-0.5% MXene exhibits a depressed semicircle at high frequencies as compared to the pure CdS nanosheets. This consolidates that the introduction of Ti<sub>3</sub>C<sub>2</sub>T<sub>x</sub> with metallic conductivity contributes to the enhanced charge transfer process, which is further collaborated by the cyclic voltammetry (CV) curves (Fig. S13) and the polarization curves (Fig. S14). The above results together demonstrate that the introduction of Ti<sub>3</sub>C<sub>2</sub>T<sub>x</sub> effectively enhances the separation and transfer of photogenerated charge carriers of CdS, thereby improving the extraction of photogenerated electrons. Benefiting from this merit along with the exposed surface reaction sites ensured by the 2D-2D heterostructure, the photoreduction activity of 4-NA over CdS/Ti<sub>3</sub>C<sub>2</sub>T<sub>x</sub> is improved (Fig. 3e).

The photocorrosion has been recognized to deteriorate the stability of CdS, which is due to the photogenerated holes induced oxidation of S<sup>2-</sup>, accompanied by the release of Cd<sup>2+</sup> ions [47,48]. To test the stability of the as-prepared samples, recycling tests have been performed. From Fig. 4a it can be seen that the reduction of 4-NA over the pure CdS nanosheets gradually decreases, which suggests that the addition of ammonium formate as hole scavengers cannot completely prohibit the photocorrosion of CdS. This can be ascribed to the slow transfer of the photogenerated holes from the bulk of CdS to the surface and their surface reactions with electron donors of ammonium formate [31,32]. In sharp contrast, CdS-0.5% MXene exhibits improved stability for the conversion of 4-NA. To probe the evident difference in the stability of these two samples, X-ray photoelectron spectroscopy (XPS) analysis of

the used CdS nanosheets and CdS-0.5% MXene has been performed. As shown in Fig. 4b, the S 2p peak can be deconvoluted into two doublets for the used CdS nanosheets and CdS-0.5% MXene. The doublet located at 160.0–162.0 eV can be assigned to S<sup>2-</sup>, while the doublet positioned at higher binding energy (between 162.0 and 164.0 eV) can be associated to polysulfides existing as S<sub>x</sub><sup>2-</sup> (x = 2–8) [49]. However, the XPS peaks of elemental sulfur (S<sup>0</sup>, 2p<sub>3/2</sub> at 163.6 eV and 2p<sub>1/2</sub> at 164.7 eV [30]) are not present, implying that the oxidation of S<sup>2-</sup> forms polysulfides instead of S<sup>0</sup> through the reaction of  $x\text{CdS} + (2x-2)\text{h}^+ \rightarrow x\text{Cd}^{2+} + \text{S}_x^{2-}$  in the present system. Among the existing sulfur species, the S<sub>x</sub><sup>2-</sup> ratio is calculated to be 26.0% for the CdS nanosheets, while it decreases to 17.1% for CdS-0.5% MXene, revealing the retarded photocorrosion of CdS by the introduction of Ti<sub>3</sub>C<sub>2</sub>T<sub>x</sub>.

To gain a deeper insight into the effect of Ti<sub>3</sub>C<sub>2</sub>T<sub>x</sub> on enhancing the photostability of CdS, Cd<sup>2+</sup> leakage under visible light irradiation has been measured. As shown in Fig. 4c, for the pure CdS nanosheets, the concentration of Cd<sup>2+</sup> apparently increases with prolonged light irradiation time. For CdS-0.5% MXene, although intrinsic photocorrosion occurred as indicated by the presence of S<sub>x</sub><sup>2-</sup> from the above XPS results, the leaching of Cd<sup>2+</sup> is negligible within 5 h. Fig. 4d shows the Cd<sup>2+</sup> adsorption results over Ti<sub>3</sub>C<sub>2</sub>T<sub>x</sub> and CdS nanosheets in the dark. Ti<sub>3</sub>C<sub>2</sub>T<sub>x</sub> exhibits effective adsorption toward Cd<sup>2+</sup> and a Cd<sup>2+</sup> uptake of 23.2 mg g<sup>-1</sup> is achieved over Ti<sub>3</sub>C<sub>2</sub>T<sub>x</sub>. As for the case of CdS nanosheets, the concentration of Cd<sup>2+</sup> remains almost unchanged in the initial stage, while it increases with prolonged time. This suggests that CdS nanosheets cannot effectively adsorb Cd<sup>2+</sup> but will gradually dissolve in water.

The Cd<sup>2+</sup> leaching measurements under light irradiation ( $\lambda \geq 420$  nm) and the Cd<sup>2+</sup> adsorption experiments in the dark indicate that there is a strong adsorption affinity between Ti<sub>3</sub>C<sub>2</sub>T<sub>x</sub> and Cd<sup>2+</sup> due to the high binding energy of Cd<sup>2+</sup> on Ti<sub>3</sub>C<sub>2</sub>T<sub>x</sub> [50]. As illustrated in Fig. 5, this leads to the local confinement of photocorrosion-released Cd<sup>2+</sup> around CdS instead of rapid diffusion into the solution, thereby slowing down the hole-induced photocorrosion of CdS according to Le Chatelier's principle [51]. The 2D-2D stacking realized by the electrostatic assembly in the present study endows the intimate interaction between CdS nanosheets and Ti<sub>3</sub>C<sub>2</sub>T<sub>x</sub>, which is beneficial to exerting the "Cd<sup>2+</sup> confinement effect" of Ti<sub>3</sub>C<sub>2</sub>T<sub>x</sub>, thus affording stability enhancement of CdS-based photocatalysts. It is also worth noting that, being distinctly different from previous strategies using surface coating barriers to isolate CdS from the reaction mediums, and vice versa, the reactants [29,30], this new concept to retard the CdS photocorrosion through local Cd<sup>2+</sup> confinement on the intimately interlayer interacted Ti<sub>3</sub>C<sub>2</sub>T<sub>x</sub> ensures accessible surface reaction sites and diminishes the barriers for mass transfer, which allows sufficient interactions with reactants and is of crucial importance to determine photocatalytic activities.

#### 4. Conclusions

In conclusion, we have prepared 2D CdS/Ti<sub>3</sub>C<sub>2</sub>T<sub>x</sub> heterostructures with well-defined interfaces and open surface reaction sites toward stable CdS-based photocatalysts with enhanced visible light photoactivity. Ti<sub>3</sub>C<sub>2</sub>T<sub>x</sub> facilitates the separation and transfer of photogenerated electrons, thereby improving the photoactivity of CdS. With the concurrent contribution of Ti<sub>3</sub>C<sub>2</sub>T<sub>x</sub> to *in situ* confine Cd<sup>2+</sup> ions to avoid their leaching, the photogenerated holes induced photocorrosion of CdS is restrained, thus leading to the enhanced photostability of CdS. This provides new mechanistic insights into retarding the photocorrosion of CdS-based photocatalysts by preventing Cd<sup>2+</sup> leaching but without compromising surface reaction sites. With these merits, Ti<sub>3</sub>C<sub>2</sub>T<sub>x</sub> MXene serves as a Janus cocatalyst to regulate the reactions with electrons and those with holes toward concurrently improving the photoactivity and stability of CdS. This work would be expected to bring new conceptual idea to the design of efficient and stable photocatalysts for sustainable solar energy conversion.

## Acknowledgements

The support from the NSFC (U14463204 and 21173045), the Award Program for Minjiang Scholar Professorship, the Independent Research Project of State Key Laboratory of Photocatalysis on Energy and Environment (NO. 2014A05), the 1st Program of Fujian Province for Top Creative Young Talents, the Natural Science Foundation (NSF) of Fujian Province for Distinguished Young Investigator Rolling Grant (2017J07002), the Program for Returned High-Level Overseas Chinese Scholars of Fujian province, and the China Postdoctoral Science Foundation (2018M630727) is gratefully acknowledged.

## Appendix A. Supplementary data

Supplementary material related to this article can be found, in the online version, at doi:<https://doi.org/10.1016/j.apcatb.2018.05.070>.

## References

- [1] J.C. Colmenares, R. Luque, Chem. Soc. Rev. 43 (2014) 765–778.
- [2] N. Zhang, M.-Q. Yang, S. Liu, Y. Sun, Y.-J. Xu, Chem. Rev. 115 (2015) 10307–10377.
- [3] N. Zhang, C. Han, Y.-J. Xu, J.J. Foley Iv, D. Zhang, J. Codrington, S.K. Gray, Y. Sun, Nat. Photon. 10 (2016) 473–482.
- [4] Q. Yuan, D. Liu, N. Zhang, W. Ye, H. Ju, L. Shi, R. Long, J. Zhu, Y. Xiong, Angew. Chem. Int. Ed. 56 (2017) 4206–4210.
- [5] N. Zhang, C. Han, X. Fu, Y.-J. Xu, Chem. (2018), <http://dx.doi.org/10.1016/j.chempr.2018.05.005>.
- [6] J.-D. Xiao, L. Han, J. Luo, S.-H. Yu, H.-L. Jiang, Angew. Chem. Int. Ed. 57 (2018) 1103–1107.
- [7] G. Zhao, Y. Sun, W. Zhou, X. Wang, K. Chang, G. Liu, H. Liu, T. Kako, J. Ye, Adv. Mater. 29 (2017) 1703258.
- [8] H. Li, Y. Zhou, W. Tu, J. Ye, Z. Zou, Adv. Funct. Mater. 25 (2015) 998–1013.
- [9] D. Wang, T. Hisatomi, T. Takata, C. Pan, M. Katayama, J. Kubota, K. Domen, Angew. Chem. Int. Ed. 52 (2013) 11252–11256.
- [10] A. Li, X. Chang, Z. Huang, C. Li, Y. Wei, L. Zhang, T. Wang, J. Gong, Angew. Chem. Int. Ed. 55 (2016) 13734–13738.
- [11] M. Xing, B. Qiu, M. Du, Q. Zhu, L. Wang, J. Zhang, Adv. Funct. Mater. 27 (2017) 1702624.
- [12] H. Yan, J. Yang, G. Ma, G. Wu, X. Zong, Z. Lei, J. Shi, C. Li, J. Catal. 266 (2009) 165–168.
- [13] Q. Li, B. Guo, J. Yu, J. Ran, B. Zhang, H. Yan, J.R. Gong, J. Am. Chem. Soc. 133 (2011) 10878–10884.
- [14] S. Navalón, A. Dhakshinamoorthy, M. Álvaro, H. Garcia, ChemSusChem 6 (2013) 562–577.
- [15] J. Chen, X.-J. Wu, L. Yin, B. Li, X. Hong, Z. Fan, B. Chen, C. Xue, H. Zhang, Angew. Chem. Int. Ed. 54 (2015) 1210–1214.
- [16] G. Han, Y.-H. Jin, R.A. Burgess, N.E. Dickenson, X.-M. Cao, Y. Sun, J. Am. Chem. Soc. 139 (2017) 15584–15587.
- [17] M.F. Kuehnel, K.L. Orchard, K.E. Dalle, E. Reisner, J. Am. Chem. Soc. 139 (2017) 7217–7223.
- [18] Z.-R. Tang, B. Han, C. Han, Y.-J. Xu, J. Mater. Chem. A 5 (2017) 2387–2410.
- [19] S. Guan, X. Fu, Y. Zhang, Z. Peng, Chem. Sci. 9 (2018) 1574–1585.
- [20] W. Jiang, Y. Liu, R. Zong, Z. Li, W. Yao, Y. Zhu, J. Mater. Chem. A 3 (2015) 18406–18412.
- [21] Y.P. Xie, Z.B. Yu, G. Liu, X.L. Ma, H.-M. Cheng, Energy Environ. Sci. 7 (2014) 1895–1901.
- [22] K. Li, M. Han, R. Chen, S.-L. Li, S.-L. Xie, C. Mao, X. Bu, X.-L. Cao, L.-Z. Dong, P. Feng, Y.-Q. Lan, Adv. Mater. 28 (2016) 8906–8911.
- [23] J. Hu, A. Liu, H. Jin, D. Ma, D. Yin, P. Ling, S. Wang, Z. Lin, J. Wang, J. Am. Chem. Soc. 137 (2015) 11004–11010.
- [24] H. Zhang, Y. Zhu, J. Phys. Chem. C 114 (2010) 5822–5826.
- [25] R. Peng, C.-M. Wu, J. Baltrusaitis, N.M. Dimitrijevic, T. Rajh, R.T. Koodali, Chem. Commun. 49 (2013) 3221–3223.
- [26] M. Seol, J.-W. Jang, S. Cho, J.S. Lee, K. Yong, Chem. Mater. 25 (2013) 184–189.
- [27] F.-X. Xiao, J. Miao, B. Liu, J. Am. Chem. Soc. 136 (2014) 1559–1569.
- [28] C. Han, Z. Chen, N. Zhang, J.C. Colmenares, Y.-J. Xu, Adv. Funct. Mater. 25 (2015) 221–229.
- [29] Y.-H. Yang, N. Ren, Y.-H. Zhang, Y. Tang, J. Photochem. Photobiol. A: Chem. 201 (2009) 111–120.
- [30] M. Wang, L. Cai, Y. Wang, F. Zhou, K. Xu, X. Tao, Y. Chai, J. Am. Chem. Soc. 139 (2017) 4144–4151.
- [31] K. Wu, Z. Chen, H. Lv, H. Zhu, C.L. Hill, T. Lian, J. Am. Chem. Soc. 136 (2014) 7708–7716.
- [32] T. Simon, N. Bouchonville, M.J. Berr, A. Vaneski, A. Adrović, D. Volbers, R. Wyrwich, M. Döblinger, A.S. Susha, A.L. Rogach, F. Jäckel, J.K. Stolarczyk, J. Feldmann, Nat. Mater. 13 (2014) 1013.
- [33] C. Wang, L. Wang, J. Jin, J. Liu, Y. Li, M. Wu, L. Chen, B. Wang, X. Yang, B.-L. Su, Appl. Catal. B: Environ. 188 (2016) 351–359.
- [34] D.J. Fermín, E.A. Ponomarev, L.M. Peter, J. Electroanal. Chem. 473 (1999) 192–203.
- [35] F. Ma, Y. Wu, Y. Shao, Y. Zhong, J. Lv, X. Hao, Nano Energy 27 (2016) 466–474.
- [36] M. Naguib, M. Kurtoglu, V. Presser, J. Lu, J. Niu, M. Heon, L. Hultman, Y. Gogotsi, M.W. Barsoum, Adv. Mater. 23 (2011) 4248–4253.
- [37] B. Anasori, M.R. Lukatskaya, Y. Gogotsi, Nat. Rev. Mater. 2 (2017) 16098.
- [38] J. Ran, G. Gao, F.-T. Li, T.-Y. Ma, A. Du, S.-Z. Qiao, Nat. Commun. 8 (2017) 13907.
- [39] R. Bera, S. Kundu, A. Patra, ACS Appl. Mater. Interfaces 7 (2015) 13251–13259.
- [40] J. Low, S. Cao, J. Yu, S. Wageh, Chem. Commun. 50 (2014) 10768–10777.
- [41] Y. Xu, W. Zhao, R. Xu, Y. Shi, B. Zhang, Chem. Commun. 49 (2013) 9803–9805.
- [42] M. Ghidiu, M.R. Lukatskaya, M.-Q. Zhao, Y. Gogotsi, M.W. Barsoum, Nature 516 (2014) 78–81.
- [43] X. Xie, M.-Q. Zhao, B. Anasori, K. Maleski, C.E. Ren, J. Li, B.W. Byles, E. Pomerantseva, G. Wang, Y. Gogotsi, Nano Energy 26 (2016) 513–523.
- [44] W. Wu, G. Liu, Q. Xie, S. Liang, H. Zheng, R. Yuan, W. Su, L. Wu, Green Chem. 14 (2012) 1705–1709.
- [45] A.A. Jbarah, R. Holze, J. Solid State Electrochem. 10 (2006) 360–372.
- [46] F.-X. Xiao, Z. Zeng, B. Liu, J. Am. Chem. Soc. 137 (2015) 10735–10744.
- [47] D. Meissner, C. Bennendorf, R. Memming, Appl. Surf. Sci. 27 (1987) 423–436.
- [48] N. Bao, L. Shen, T. Takata, K. Domen, Chem. Mater. 20 (2007) 110–117.
- [49] X. Yu, A. Manthiram, Adv. Energy Mater. 7 (2017) 1700561.
- [50] J. Guo, Q. Peng, H. Fu, G. Zou, Q. Zhang, J. Phys. Chem. C 119 (2015) 20923–20930.
- [51] R. Fernandez-Prini, J. Chem. Educ. 59 (1982) 550–553.